Infinite-range exterior complex scaling as a perfect absorber in time-dependent problems

Armin Scrinzi*
Ludwig Maximilians University, Theresienstrasse 37, D-80333 Munich, Germany and
Wolfgang Pauli Institute, A-1090 Vienna, Austria
(Received 15 February 2010; published 24 May 2010)

We introduce infinite range exterior complex scaling (irECS) which provides for complete absorption of outgoing flux in numerical solutions of the time-dependent Schrödinger equation with strong infrared fields. This is demonstrated by computing high harmonic spectra and wave-function overlaps with the exact solution for a one-dimensional model system and by three-dimensional calculations for the H atom and an Ne atom model. We lay out the key ingredients for correct implementation and identify criteria for efficient discretization.

DOI: 10.1103/PhysRevA.81.053845 PACS number(s): 42.50.Hz, 02.60.Cb, 33.20.Xx

I. INTRODUCTION

The absorption of outgoing parts of the wave function at the boundaries of a finite volume is a key problem for any efficient numerical solution of the time-dependent Schrödinger equation (TDSE) and it has been amply dealt with also in recent literature (see, e.g., [1] and references therein). This interest has been renewed in the context of intense laser-matter interactions: speaking in terms of physics, strong fields lead to large ionization and therefore large fluxes out of a central region. For strong-field-induced electronic and nuclear dynamics in atoms and molecules and high harmonic generation, electrons far from the system play no role and can be disregarded. When solving the TDSE for these processes, one can therefore identify an inner region (a finite volume) where an exact solution is of interest. Outside that region one must, by some means, truncate the solution without compromising the inner region. This is particularly important for higher-dimensional problems involving two or more electrons to control the size of the discretization. Out of the large number of approaches toward that goal the majority of computations of strong laser-matter interactions employed one of the following methods: absorbing masks [2], complex absorbing potentials (CAP's) [3], and exterior complex scaling (ECS) [4,5].

None of these methods appeared to be completely satisfactory: absorbing masks and the closely related CAP's require careful adaptation to a given problem and a comparatively large absorption range, but still do not allow perfect absorption. As to ECS, the two recent numerical studies have cast doubt on the efficiency [5] and maybe even the fundamental correctness the method in numerical practice [4]: rather poor accuracies, problems with numerical stability, apparent fundamental limitations of long-range absorption, and also poor efficiency were reported.

Here we present infinite range ECS (irECS) which turns ECS into a perfect absorber: Instead of applying ECS on a finite discretization range, the absorbing part of the wave functions is discretized by a finite number of basis functions with infinite extension. We will show that with this comparatively simple modification absorption to full computational accuracy (14 digits) using only a small fraction of the total discretization points is achieved. The method far outperforms conventional ECS and the commonly used monomial CAP's. In addition, irECS is not just an absorber: Ideally, it keeps a record of the dynamics in the outer region, which, in principle, can be recovered. We will provide numerical evidence for this behavior that was conjectured based on formal arguments in Ref. [6].

After giving a brief review of general ECS theory, we will present with some care our discretization method, as it plays an important role in irECS. The general characterization of irECS and a comparison with ECS and CAP's is done using a one-dimensional model system, and finally we will present results in three dimensions for the H atom and a single-electron model of Ne.

II. TDSE WITH A LASER FIELD

We want to solve the TDSE of the general form

$$i\frac{d}{dt}\Psi(\vec{x},t)=\left[-\frac{1}{2}\Delta_{\vec{x}}+i\vec{A}(t)\cdot\vec{\nabla}_{\vec{x}}+V(\vec{x})\right]\Psi(\vec{x},t), \quad (1)$$

where $\vec{x}$ will be either a single x or three x,y,z spatial coordinates. $\Delta_{\vec{x}},\vec{\nabla}_{\vec{x}}$ then denote $\frac{\partial^2}{\partial\vec{x}^2},\frac{\partial}{\partial\vec{x}}$ and the Laplace and Nabla operators, respectively. $V(\vec{x})$ is a system-dependent binding potential and $\vec{A}(t)$ is the vector potential of the laser field. Here we have chosen the velocity gauge and removed the term $A(t)^2/2$ by a time-dependent unitary transform. Here and throughout the paper we use atomic units (a.u.) $e^2=\hbar=m_e=1$ unless indicated otherwise. As the initial state we use the lowest-energy eigenfunction of the field-free Hamiltonian operator $-\frac{1}{2}\Delta+V$. We use vector potentials with finite duration

$$\vec{A}(t)=\vec{A}_0\cos^2\left(\frac{\pi t}{2nT}\right)\sin\left(\frac{2\pi t}{T}\right), \quad (2)$$

in the time interval $[-nT,nT]$ with $n=1,5,10$. The peak vector potential is $\vec{A}_0=A_0$ and $\vec{A}_0=(A_0,0,0)$ in one and three dimensions, respectively. Such pulses with a single or a few oscillations of the electric field, linear polarization, and peak field amplitude at $t=0$ are frequently used as models in numerical studies.

The complete information of the system inside some inner region $|\vec{x}|\leqslant R_0$ is contained in the wave-function amplitude. For characterizing the accuracy of our results by a single

*armin.scrinzi@lmu.de

number, we use the overlap between an "exact" solution $\Psi_{\rm ex}$ obtained from a calculation in a very large box and the approximate solution Ψ

$$\mathcal{E}^2[B] = 1 - \frac{|\langle\Psi_{\rm ex}|\Psi\rangle_B|^2}{||\Psi_{\rm ex}||_B^2||\Psi||_B^2}. \tag{3}$$

The scalar product is restricted to the inner region or a subregion of the inner region $B \subset \{|\vec{x}| \leqslant R_0\}$

$$\langle\Psi_{\rm ex}|\Psi\rangle_B = \int_B dx^{(d)}\Psi_{\rm ex}^*(\vec{x})\Psi(\vec{x}), \tag{4}$$

and $||\cdot||_B$ is the corresponding $\mathcal{L}^2$ norm.

A quantity of immediate physical interest is the intensity spectrum of the harmonic response given by the Fourier transform of the "acceleration of the dipole"

$$\mathcal{S}_\Psi(\omega) = \left\{\mathcal{F}\left[\langle\Psi(\vec{x},t)|\frac{\partial V}{\partial x}|\Psi(\vec{x},t)\rangle_B\right]\right\}^2. \tag{5}$$

For the comparison, integrals are restricted to the inner region B. In general, $\mathcal{S}(\omega)$ is a highly oscillatory quantity varying by several orders of magnitude. The local error of the spectrum relative to an "exact" spectrum is

$$\mathcal{D}(\omega) = \frac{\delta\omega[\mathcal{S}_\Psi(\omega) - \mathcal{S}_{\Psi_{\rm ex}}(\omega)]}{\int_{\omega-\delta\omega}^{\omega+\delta\omega} d\omega\mathcal{S}_\Psi(\omega)}. \tag{6}$$

Local averaging in the denominator suppresses spurious spikes due to the near-zeros of the spectrum.

III. OUTLINE OF GENERAL ECS THEORY

There is a large volume of literature available on complex scaling in general (see, e.g., [7–9]) and on exterior complex scaling in particular (see, e.g., [10–12], and references therein). We restrict our summary to communicating the basic idea and to emphasizing the points that are essential for correct numerical implementation. For this we closely follow the earlier work found in Ref. [13]. In one dimension, exterior complex scaling consists in continuing the coordinate outside a "scaling radius" R_0 into the complex plane

$$x \to z_{\theta R_0}(x) = \begin{cases} x & \text{for } |x| < R_0 \\ e^{i\theta}(x \pm R_0) \mp R_0 & \text{for } \mp x > R_0. \end{cases} \tag{7}$$

The effect of the transformation on plane waves at values $x > R_0$ is

$$e^{\pm ipx} \to e^{\pm ipR_0}e^{\pm ip\cos\theta(x-R_0)}e^{\mp p\sin\theta(x-R_0)}. \tag{8}$$

For positive p—outgoing waves to the right side—the functions become exponentially damped with increasing x, while for negative p they grow exponentially. The corresponding situation with reversed signs arises for $x < -R_0$. By complex scaling we can distinguish incoming from outgoing waves simply by their normalizibility without the need to analyze the asymptotic phase. In a typical discretization we implicitly or explicitly use only square-integrable functions, by which we exclude incoming waves from a complex-scaled calculation. This is the key to complex scaling as a perfect absorber: in a well-defined region we have a simple instrument to systematically suppress incoming waves by just requiring that our solution remain square integrable. A more elaborate version of this reasoning can be found in the Appendix of Ref. [14].

The mathematically rigorous theory of complex scaling often uses the alternative point of view that not the wave functions, but rather the operator itself is scaled, while it remains an operator acting on an ordinary Hilbert space of square-integrable functions. We follow this line of reasoning for pointing out a fact of immediate computational relevance. We only give here plausibility arguments and refer the reader to Ref. [13] for a more extensive discussion and references to mathematical literature.

One starts from *real* scaling, that is, replacing $i\theta$ in Eq. (7) with a real number λ and observes that the transformation

$$(U_{\lambda R_0}\Psi)(x) = \begin{cases} \Psi(x) & \text{for } x < R_0 \\ e^{\lambda/2}\Psi\big(e^\lambda(x \mp R_0) \mp R_0\big) & \text{for } \mp x > R_0, \end{cases} \tag{9}$$

is unitary. The scaling factor $e^{\lambda/2}$ is essential to ensure unitarity. Formally, this transform can just as well be applied to the Hamiltonian by defining

$$H_{\lambda R_0} := U_{\lambda R_0} H U_{\lambda R_0}^*. \tag{10}$$

It is important to note that if H is defined on differentiable functions Ψ, the transformed operator is defined on the *discontinuous* functions $\Psi_{\lambda R_0} = U_{\lambda R_0}\Psi$ and its action on these functions is given by

$$H_{\lambda R_0}\Psi_{\lambda R_0} = U_{\lambda R_0} H U_{\lambda R_0}^*\Psi_{\lambda R_0} = U_{\lambda R_0} H\Psi. \tag{11}$$

As a unitary transform $U_{\lambda R_0}$ leaves the operator's spectrum unchanged and the scaled dynamics are in a one-to-one relation to the unscaled. Now the hard part of the mathematical theory sets in: For a certain class of "dilation analytic" potentials, the operators $H_{\lambda R_0}$ can be analytically continued to complex values $\lambda \to i\theta$ without changes in the bound-state spectrum [9]. The continuous spectrum is rotated around the continuum threshold into the lower complex energy plane by the angle 2θ. This is trivial to see for the free particle and the case $R_0 = 0$ where the spectrum $\sigma(-\Delta)$ transforms as

$$\sigma(-\Delta) = [0,\infty) \to \sigma(-e^{-2i\theta}\Delta) = [0, e^{-2i\theta}\infty). \tag{12}$$

This property of the continuous spectrum persists when dilation analytic potentials are added and for $R_0 > 0$: the complex-scaled Hamiltonian retains a distinct "memory" of the unscaled Hamiltonian. Proof of dilation analyticity can be difficult to find. Beyond some large R_0, where most physical potentials have simple decaying tails, the expected properties of ECS can be confirmed by the numerical experiment.

One can now write an exterior complex-scaled TDSE

$$\begin{aligned} i\frac{d}{dt}&\Psi_{\theta R_0}(x,t) \\ &= H_{\theta R_0}(t)\Psi_{\theta R_0}(x,t) \\ &= \left[-\frac{1}{2}\Delta_{\theta R_0} + i\vec{A}(t)\cdot\vec{\nabla}_{\theta R_0} + V_{\theta R_0}(x)\right]\Psi_{\theta R_0}(x,t). \end{aligned} \tag{13}$$

Here it is assumed that the potential can be analytically continued to complex values $V_{\theta R_0}(x) = V[z_{\theta R_0}(x)]$. One may

hope that the dynamics generated by (13) are related to the original dynamics and that for $|x| < R_0$ the solution is identical to the unscaled solution $\Psi_{\theta R_0}(\vec{x}) = \Psi(\vec{x})$. We will demonstrate in the following that this expectation can be confirmed by numerical experiment to the level of full machine precision.

The main purpose of this brief discussion of ECS theory is to stress the importance of the correct discontinuity in the wave function for defining differential operators. The discontinuity at R_0 is intimately linked to the unitarity of the real-scaled problem, which in turn secures the conservation of spectral properties of the scaled operator. For given R_0 and θ it has the explicit form

$$\Psi_{\theta R_0}(R_0 - 0) = e^{i\theta/2}\Psi_{\theta R_0}(R_0 + 0), \tag{14}$$

$$\Psi'_{\theta R_0}(R_0 - 0) = e^{i3\theta/2}\Psi'_{\theta R_0}(R_0 + 0). \tag{15}$$

The discontinuity condition (15) on the derivative arises from transforming the continuous first derivatives of the original functions. On such functions, one can define the complex-scaled Laplacian in analogy to Eq. (11) by "back-scaling" the scaled function $\Psi_{\theta R_0}(x) \to \Psi_{\theta R_0}(e^{-i\theta}(x \mp R_0) \pm R_0)$, applying the ordinary Laplacian, and forward-scaling the result

$$(\Delta_{\theta R_0}\Psi_{\theta R_0})(x) = \begin{cases} \Delta\Psi_{\theta R_0}(x) & \text{for } |x| < R_0 \\ e^{-2i\theta}\Delta\Psi_{\theta R_0}(x) & \text{for } |x| > R_0. \end{cases} \tag{16}$$

The factor $e^{-2i\theta}$ appears, as the derivative $\partial^2/\partial x^2$ is applied to the back-scaled function rather than to $\Psi_{\theta R_0}(x)$. On continuous functions the scaled Laplacian (and any derivative) is not defined as an operator in the Hilbert space, just as an ordinary Laplacian is not defined on discontinuous functions.

Finally, we want to point to the fact that the adjoint operator $(\Delta_{[0,\theta]})^\dagger = \Delta_{[0,-\theta]}$ requires functions with the complex conjugate condition of Eqs. (14) and (15). This means that for our discretization by a basis set the discontinuities *must not be conjugated* when going from ket to bra vectors. We will show in what follows how this can be easily implemented in a finite element basis.

IV. DISCRETIZATION OF IRECS

For the discretization three points are crucial: (i) the correct implementation of the discontinuity, (ii) the use of infinite range functions, and (iii) good approximation of analyticity. All can be most conveniently accommodated in a finite element discretization of high rank.

We follow the implementation strategy laid out in Ref. [13]: each coordinate axis is divided into N elements $[x_{n-1},x_n]$, $n = 1,\ldots,N$. On each element with number n, we choose a set of p_n linearly independent functions $f_i^{(n)}, i = 1,\ldots,p_n$ that can be transformed such that all functions are equal to zero at x_{n-1} and x_n, except for the first and last functions, which have values equal to one at the lower and upper element boundaries, respectively,

$$\begin{aligned} f_i^{(n)}(x_{n-1}) = f_i^{(n)}(x_n) = 0, \\ \text{except } f_1^{(n)}(x_{n-1}) = f_{p_n}^{(n)}(x_n) = 1. \end{aligned} \tag{17}$$

We will call p_n the "rank" of the finite element. In principle, any set of functions that obeys (17) can be used in a finite element scheme. In practice we use real-valued polynomials which, for enhancing numerical stability, we transform to

$$\int_{x_n-1}^{x_n} f_i^{(n)}(x) f_j^{(n)}(x)dx = m_i^{(n)}\delta_{ij} \quad \forall ij \neq 1p_n, p_n 1, \tag{18}$$

with normalization constants $m_i^{(n)}$. A brief technical discussion of the transformations needed to arrive at Eq. (18) is given in the Appendix.

For the element functions (17), Dirichlet boundary conditions are implemented by omitting the first and last functions $f_1^{(1)}$ and $f_{p_N}^{(N)}$ on the first and last elements of the simulation box, respectively. Alternatively, on the leftmost and rightmost intervals we use polynomials times an exponential $e^{\pm\alpha x}$ with $+$ and $-$ signs on the intervals $(-\infty,x_1]$ and $[x_{N-1},\infty)$, respectively. The conditions on the end-element functions are

$$\begin{aligned} f_i^{(1)}(x_1) = 0 \quad \text{except} \quad f_{p_1}^{(1)}(x_1) = 1, \\ f_i^{(N)}(x_{N-1}) = 0 \quad \text{except} \quad f_1^{(N)}(x_{N-1}) = 1. \end{aligned} \tag{19}$$

The exponent α can be adjusted for best performance, but its exact value was found to be uncritical for irECS.

The finite-element ansatz for the total wave function is as usual

$$\Psi(x,t) = \sum_{n=1}^{N}\sum_{i=1}^{p_n} c_i^{(n)}(t) f_i^{(n)}(x). \tag{20}$$

By construction of the $f_i^{(n)}$, Eq. (17), continuity across element boundaries is assured by demanding

$$c_{p_{n-1}}^{(n-1)} = c_1^{(n)}, \quad n = 2,\ldots,N. \tag{21}$$

Elementwise overlap and Hamiltonian matrices are

$$S_{ij}^{(n)} = \int_{x_{n-1}}^{x_n} J(x)\left[f_i^{(n)}(x)\right]^* f_j^{(n)}(x)dx, \tag{22}$$

$$H_{ij}^{(n)} = \int_{x_{n-1}}^{x_n} J(x)\left[f_i^{(n)}(x)\right]^* H(t) f_j^{(n)}(x)dx, \tag{23}$$

where $J(x)$ denotes the Jacobian function for integration over x. The elementwise matrices are added into the overall discretized matrices $\hat{H}$ and $\hat{S}$ such that the last row and column of each elementwise matrix overlaps with the first row and column of the following element (see Fig. 1), which is equivalent to setting the corresponding coefficients equal, Eq. (21). As always in finite element methods, continuity of the first derivative does not need to be imposed (see Ref. [13] for a more detailed discussion). $\hat{H}$ and $\hat{S}$ are $M \times M$ matrices with

$$M = \begin{cases} \sum_{n=1}^{N} p_n - N - 1 & \text{for all } |x_n| < \infty \\ \sum_{n=1}^{N} p_n - N + 1 & \text{for } |x_0| = |x_N| = \infty. \end{cases} \tag{24}$$

For irECS we choose the scaling radii to coincide with the element boundaries $x_{n\pm} = \pm R_0$. The scaled elementwise Hamiltonian matrices are evaluated by substituting in (23) the Jacobian $J(x)$ and the operator $H(t)$ with their ECS equivalents

$$H_{\theta R_0,ij}^{(n)} = \begin{cases} \int_{x_{n-1}}^{x_n} dx\, J f_i^{(n)} H f_j^{(n)} & |x| < R_0 \\ e^{i\theta}\int_{x_{n-1}}^{x_n} dx\, J_{\theta R_0} f_i^{(n)} H_{\theta R_0} f_j^{(n)} & |x| > R_0. \end{cases} \tag{25}$$

$$\begin{pmatrix}
\ddots & \vdots & \vdots & \vdots & \vdots \\
\ddots & H^{(n-1)}_{p_{n-1}-1p_{n-1}} & 0 & 0 & 0 \\
\cdots & H^{(n-1)}_{p_{n-1}p_{n-1}}+H^{(n)}_{11} & \cdots & H^{(n)}_{n} & 0 \\
0 & H^{(n)}_{21} & \ddots & H^{(n)}_{2p_n} & 0 \\
\vdots & \vdots & \ddots & \vdots & \vdots \\
0 & H^{(n)}_{p_n-11} & \cdots & H^{(n)}_{p_{n-1}p_n} & 0 \\
0 & H^{(n)}_{p_n1} & \cdots & H^{(n)}_{p_np_n}+H^{(n+1)}_{11} & H^{(n+1)}_{12} \\
0 & 0 & 0 & H^{(n+1)}_{21} & \ddots \\
\vdots & \vdots & \vdots & \vdots & \ddots
\end{pmatrix}$$

FIG. 1. Placement of the elementwise block $H^{(n)}_{ij}$ in the overall Hamiltonian matrix $\hat{H}$.

As we use *real* functions $f^{(n)}_i$, we can omit the complex conjugation and the resulting matrices are complex symmetric [i.e., $H^{(n)}_{\theta R_0,ij} = H^{(n)}_{\theta R_0,ji}$]. The discontinuity (14) is brought into the system by the factor $e^{i\theta}$ for the integrals $|x| > R_0$: it amounts to multiplying all functions $f^{(n)}_i$ outside the scaling radius by $e^{i\theta/2}$ and as the discontinuity does not get complex conjugated, the bra and ket discontinuity factors do not cancel but multiply to $e^{i\theta}$. As in the unscaled case, the continuity condition on the first derivative (15) does not need to be imposed for finite elements. The procedure for constructing the overall matrix $\hat{H}_{\theta R_0}$ is identical to the unscaled case. Replacing $H(t)$ by 1 results in the correct (non-Hermitian) overlap matrix $\hat{S}_{\theta R_0}$ for the discretized problem. In practice, the matrices $\hat{H}_{\theta R_0}$ and $\hat{S}_{\theta R_0}$ are rarely set up explicitly, as applying the elementwise matrices to the corresponding sections of the coefficient vectors is far more efficient.

There are no specific issues for time propagating the discretized system

$$\hat{S}_{\theta R_0}\frac{d}{dt}\vec{c} = \hat{H}_{\theta R_0}(t)\vec{c}, \tag{26}$$

except maybe that very high accuracy was needed for our comparisons. If anything, irECS mitigates the well-known stiffness problems for explicit time integrators, as high kinetic energy are also associated with large imaginary parts and decay rapidly. We use Runge-Kutta schemes with self-adaptive step size and self-adaptive order up to order 7. Robust error control is achieved by single-to-double-step comparisons. We obtain significant speedups of the propagation by removing states with very high eigenvalues of the field-free Hamiltonian from the simulation space by explicit projection.

V. IRECS FOR A ONE-DIMENSIONAL PROBLEM

We first investigate irECS for the one-dimensional "hydrogen atom" with the model potential

$$V(x) = -\frac{1}{\sqrt{2+x^2}}, \tag{27}$$

which gives the ground-state energy $-1/2$. Here and in the following we use the peak vector potential $|A_0| = 1.26$ and the optical period $T = 104.8$. If interpreted as atomic units, these parameters correspond to peak intensity 2×10^{14} W/cm^2 and wave length 760 nm. We will show results for the full width at half maximum (FWHM) of the amplitude of $n = 1$, 5, and 10 optical cycles and total pulse durations of 2, 10, and 20 optical cycles, see Eq. (2). The classical quiver amplitude of an electron in this field is $A_0 \times T/2\pi = 21$ atomic units. At the end of a single cycle pulse with this intensity around 20% and after a five cycle pulse more than 80% of the electron probability have left the range $[-40,40]$.

Within the framework of this model system we will answer the following questions: Can irECS be considered a perfect absorber? Can the scaling radius be put inside the range of the quiver motion (i.e., $R_0 < 21$)? Does irECS work for long pulses? Which parameters determine the efficiency of irECS? How does it compare to conventional ECS? How many discretization coefficients are needed? How does irECS perform compared to monomial CAP's? Does irECS work for length gauge?

A. irECS is a perfect absorber

We call an absorber perfect if the error $\mathcal{E}[-R_0,R_0]$ defined in Eq. (3) is on the level of machine precision. For the comparison we need an "exact" result Ψ_{ex}, which is obtained from an unscaled calculation on a large box $[x_2,x_{N-1}] = [-1180,1180]$ with a total of $M = 4801$ discretization coefficients distributed over 120 elements with constant rank $p_n \equiv 41$. The elements are equidistant except for the infinite end elements $x_0 = -\infty$ and $x_N = \infty$ with exponent $\alpha = 0.5$, Eq. (19).

For irECS we use the parameters $\theta = 0.5$ and $R_0 = 40$ and finite elements that up to R_0 are the same as in the unscaled calculation. In the scaled ranges on either end of the axis we use infinite elements $(\infty, -R_0]$ and $[R_0,\infty)$ with $p_1 = p_N = 41$ and exponent $\alpha = 0.5$. At this point, no attempt was made to minimize the number of coefficients used for absorption by optimizing the scaling parameters. Indeed, with the given parameters we obtain for the $\mathcal{L}^2$ errors at the end of the pulses $t = nT$

$$\mathcal{E}[-R_0,R_0] = \begin{cases} 2\times 10^{-15} & \text{for } n = 1 \\ 3\times 10^{-14} & \text{for } n = 5. \end{cases} \tag{28}$$

The error of the wave-function amplitude is about the square root of these values and it remains constant after the initial rise, see Fig. 2. The error level is constant through the whole range $[-R_0,R_0]$ and there is a sharp edge to the scaled region, where the wave function is not directly related to the unscaled one. The errors indicate the accuracy limits of our numerical integration scheme and are not determined by irECS. It is therefore fair to say that, at least for the present model, irECS acts as a perfect absorber.

B. Element rank and comparison to finite range ECS

The choice of conspicuously high element rank for these very accurate calculations is not by coincidence. Complex scaling depends on analyticity properties of the Hamiltonian. It is therefore not surprising that we observe a strong dependency of the accuracy on the degree to which our discretization can approximate analytic functions. Any localized basis, such as finite elements or B-splines is not analytic by definition

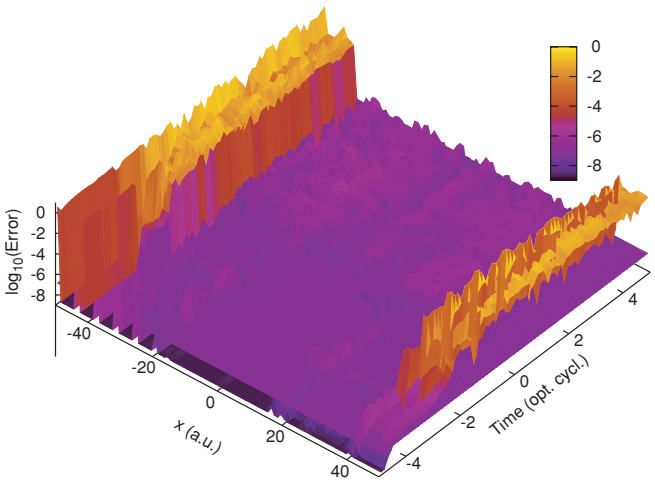

FIG. 2. (Color online) Evolution of the relative error $|\Psi(x) - \Psi_{ex}(x)|/|\Psi(x)|$ during a five-cycle pulse. The denominator is averaged over five grid points to avoid spurious spikes. For the pulse parameters and discretization see text. The sharp rise of error marks the boundaries of the inner region. A plane is drawn at error level 10^{-7} (blue); only a few error peaks in the inner region are above 10^{-6}. Away from the center, relative errors are enhanced initially as the wave function is nearly zero.

because of the finite support of the basis functions. However, with increasing polynomial degree, loosely speaking, one gets closer to analytic functions. Table I lists the error of the wave function in the range $[-35,35]$ for increasing element rank. As $\pm R_0$ must fall onto element boundaries, we had to choose slightly different values R_0 for the different element ranks. The irECS absorption range is discretized with between 36 and 45 exponentially damped functions with $\alpha = 0.4$ such that the sum of coefficients in the scaled and unscaled regions was $M = 241$ for all calculations. For the error estimates at each p_n a large box real calculation was performed with the same p_n and the same number of points as for irECS in $|x| < R_0$. From Table I we see that, depending on the desired accuracy, it is advisable to use polynomial degrees 8 or higher.

For practical purposes, we want to mention that the variation of an irECS calculation with θ and box size is not a safe indicator of its accuracy. We found irECS calculations with fixed R_0, element rank, and element sizes to be far more consistent among each other than their error relative to the unscaled result. For reliable accuracy estimates one must vary the scaling radius R_0.

TABLE I. Dependence of the final wave-function error on the element rank p_n. All ECS calculations are for a single-cycle pulse and a total of $M = 241$ discrete coefficients.

$p_n, n \neq 1, N$	$p_1 = p_N$	R_0	$\mathcal{E}[-35,35]$
4	41	40	4×10^{-8}
5	41	40	1×10^{-7}
6	41	40	3×10^{-10}
7	43	39	1×10^{-9}
9	41	40	5×10^{-12}
11	41	40	9×10^{-12}
13	37	42	2×10^{-13}
15	46	38	7×10^{-14}
21	41	40	2×10^{-15}

TABLE II. Error of ECS calculations with infinite and finite absorption ranges. In all calculations we use a single-cycle pulse, rank $p_n = 21$, and 160 discretization points in $[-R_0, R_0] = [-40,40]$. The length of the absorption range is $A = -R_0 - x_1 = x_N - R_0$ and M_A is the number of coefficients for absorption at each side.

A	M_A	$\mathcal{E}[-40,40]$
∞	21	2×10^{-15}
10	20	4×10^{-4}
20	40	3×10^{-6}
30	60	2×10^{-11}
40	80	1×10^{-15}

The use of infinite elements at the ends of the simulation box is the key to the high efficiency of irECS. Table II compares a few finite-box calculations with a calculation using infinite end elements with only 21 discretization points. Only at rather large finite boxes and a larger number of discretization points does one reach the infinite element result.

The explanation for this may be as follows: It was noticed in Ref. [5] that long wave lengths cannot be accommodated in a finite ECS region and deteriorate absorption by reflections. Such long wave lengths have very little structure and should be easily parameterizable. It seems that the exponential tail of our irECS functions is sufficient to accommodate slowly varying long wave-length parts of the ECS wave function.

C. Choice of R_0 and back-scaling

We find that the quality of the wave function in the unscaled region is not affected by the choice of the ECS radius R_0. Table III shows the errors $\mathcal{E}[-R_0, R_0]$ for $R_0 = 5$, 10, 20, and 40. The general error level in these calculations is slightly higher as we used a lower element rank of $p_n = 11$ to be able to make the two elements of the inner region small. The density of discretization points was kept constant through all calculations. We see that the error level is independent of whether the ECS radius is chosen inside $R_0 = 5,10,20$ or outside $R_0 = 40$ the classical quiver amplitude of $\alpha_0 = 21$. Errors only start to rise when the total size of the box indicated by the number of discretization points M becomes too small. This may not be surprising, if we assume that the spatial range of the dynamics remains essentially unchanged by complex scaling: if the box, be it scaled or unscaled, cannot let a

TABLE III. Dependence of the final wave-function error on ECS radius R_0 and on the total number of discretization points M.

M	R_0	$\mathcal{E}[-R_0, R_0]$
241	40	1.0×10^{-11}
201	20	5.6×10^{-12}
160	10	2.9×10^{-12}
160	5	1.5×10^{-12}
100	10	1.8×10^{-12}
80	10	1.2×10^{-6}
60	5	3.6×10^{-2}

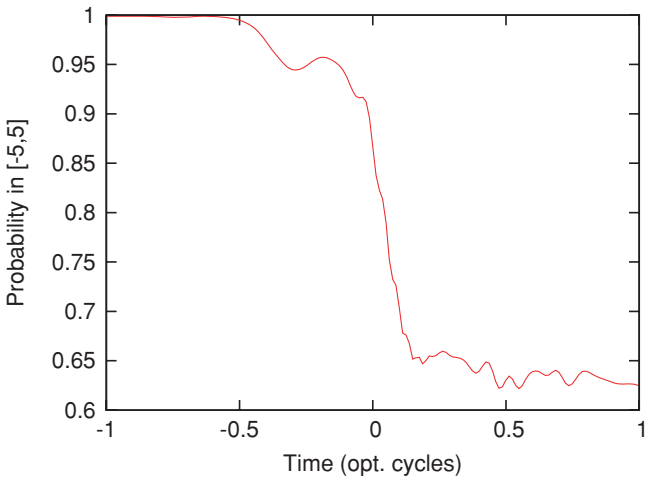

FIG. 3. (Color online) Probability of finding the electron in the interval $[-5,5]$ for the parameters used in Table III. At several times a few percent probability returns into the region.

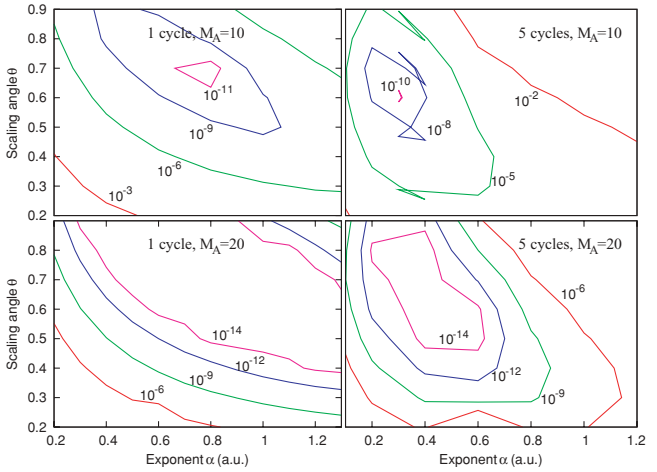

FIG. 4. (Color online) Error $\mathcal{E}[-40,40]$ as a function of scaling angle θ and exponent α for $n=1$ and $n=5$-cycle pulses. For the five-cycle pulse, longer wavelengths reach the boundaries; the optimal exponent and scaling angles are smaller and a longer (20 point) absorption range significantly increases accuracy.

particle go the full distance and then return without reflections, distortions must occur.

One can draw an interesting conclusion from the fact that the R_0 can be chosen inside the classical quiver amplitude: There is nonnegligible probability for up to a few percent for the electron to return from the scaled region (e.g., $x > R_0 = 5$) into the unscaled region (see Fig. 3). At the same time the wave function in the unscaled region never deviates from the exact wave function beyond the level of $\mathcal{E}[-5,5] < 10^{-11}$. This means that flux moves into the scaled region and then back out without corrupting the unscaled part of the wave function and that also in the scaled region the TDSE dynamics are encoded correctly, although in a different way. Our numerical results are a striking corroboration of this conjecture that was made early on in ECS theory [6]. In principle, one may hope to recover the unscaled wave function by analytic continuation. This hope for back-scaling, in fact, was the original motivation for introducing the analytic form of functions on the end elements, as an ordinary finite element function cannot be unambiguously analytically continued. We have not further pursued this possibility for two reasons. First, with larger $p_N = p_1$ and larger scaling angles θ we encountered severe numerical problems, as the back-scaled basis functions become highly oscillatory and cancellation errors destroy the reconstruction of the unscaled wave function. The second reason is the striking success of irECS with just a few points needed for absorption. It is safer and simpler to just discard the small absorption range and use the inner region directly for the evaluation of physical quantities. Yet, if for one reason or another, one wishes to back-scale a time-dependent irECS wave function, our results indicate that such a procedure can be successful. One may, in that case, use a representation of the scaled region that is less plagued by numerical problems than our exponential basis.

D. Choice of scaling angle θ and exponent α

Although with a sufficiently large absorption range one can always obtain perfect absorption independent of scaling angle θ and damping exponent α, optimizing these parameters in a given situation allows one to obtain good absorption with very few absorption points. Figure 4 shows the error $\mathcal{E}[-40,40]$ for $n=1$ and $n=5$ cycle calculations with $M_A = 10$ and 20 absorption points on either end of the interval. The exact choice of the parameters is not critical for the $M_A = 20$ calculations, where full accuracy is reached for rather large parameter ranges. As is to be expected, the five-cycle calculation with $M_A = 10$ is most sensitive to θ and α, but still in a range of $\theta = \theta_0 \pm 0.1$ and $\alpha = \alpha_0 \pm 0.1$ around the optimal values $\alpha_0, \theta_0 \approx 0.3, 0.6$ accuracy deteriorates only by two orders of magnitude to the still-acceptable value of 10^{-8}. There is a clear anticorrelation between θ and α, which may be explained looking at the oscillatory behavior of the back-scaled exponential $\mathcal{I}m \exp[-\alpha r e^{-i\theta}] = \sin[\alpha \sin\theta r]$. We conjecture that the effective back-scaled wave number $\gamma = \alpha \sin\theta$ is the relevant parameter for efficient absorption. The correlation between the parameter γ and θ nearly vanishes and optimization can safely be performed for each parameter independently.

E. Comparison to complex absorbing potentials

A popular and comparatively straightforward way of absorbing outgoing flux are complex absorbing potentials (CAP's). The basic idea is to add at the end of the simulation box a potential with a negative imaginary part, which leads to exponential damping of the wave function. In this simplest form, the method can be considered a differential form of absorption by mask functions, where at preset intervals a certain part of the wave function is removed. A fundamental limitation of these methods is that they—even in principle—cannot be strictly reflectionless. The attempt to obtain minimal reflections has led to a range of models, partially including real parts into the potential and adjusting to specific physical situations (see, e.g., [16]).

It is beyond the scope of the present work to perform a comprehensive study of CAP for the present type of problems. Rather, we use the simple and well-investigated monomial CAP's [3]

$$W(x) = -i\sigma x^q, \tag{29}$$

TABLE IV. Accuracy of irECS, ECS, and CAP for different absorption ranges A and a number of absorption coefficients M_A. Scaling angle θ and absorption strength σ for ECS and CAP, respectively, were optimized. The errors are calculated at the end of a single-cycle pulse.

Method	M_A	A	θ or σ	q	$\mathcal{E}[-R_0,R_0]$
irECS	21	∞	0.6	–	2×10^{-15}
ECS	20	10	0.6	–	2×10^{-4}
ECS	40	20	0.5	–	1×10^{-7}
CAP	20	10	10^{-4}	4	3×10^{-3}
CAP	20	10	2×10^{-6}	6	4×10^{-3}
CAP	40	20	4×10^{-6}	4	3×10^{-4}
CAP	60	30	6×10^{-7}	4	1×10^{-5}

for polynomial degrees $q=4,6$ with optimized σ in each calculation. The criterion for our comparison with irECS is the number of discretization points needed for a given level of absorption.

Results are shown in Table IV. With a finite absorption range, conventional ECS outperforms CAP roughly by one or two orders of magnitude. With irECS using only 21 absorption points, we can reach absorption to machine precision. We could not find a similar adjustment for CAP.

F. High harmonic spectra

Although the error $\mathcal{E}$ is a meaningful measure for wave-function accuracy, it cannot be directly related to the error of a given observable. Figure 5 shows the accuracy of ECS high harmonic spectra of one-cycle and five-cycle pulses relative to a real calculation. We find errors on the level between 10^{-4} and 10^{-3} and we could not get much better agreement

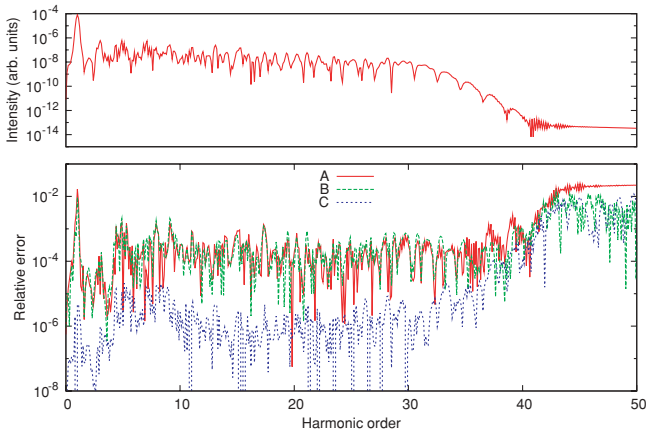

FIG. 5. (Color online) High harmonic power spectrum for a five-cycle pulse (upper panel). Lower panel: Accuracy $\mathcal{D}(\omega)$ of the high harmonic spectrum with different irECS parameters and discretizations. Curve A is the error for $(R_0,M_A,\theta,\alpha)=(40,20,0.7,0.7)$ relative to a fully converged real calculation. The choice of R_0 has the largest influence on accuracy: curve B, the difference between two calculations with $R_0=40$ and $R_0=50$ closely follows the overall error curve A. At fixed R_0 the influence of the other irECS parameters and discretization is small: curve C compares calculations using $(R_0,M_A,\theta,\alpha)=(40,20,0.7,0.7)$ and finite element rank $p_n=21$ with (40,40,0.5,0.3) and rank 41.

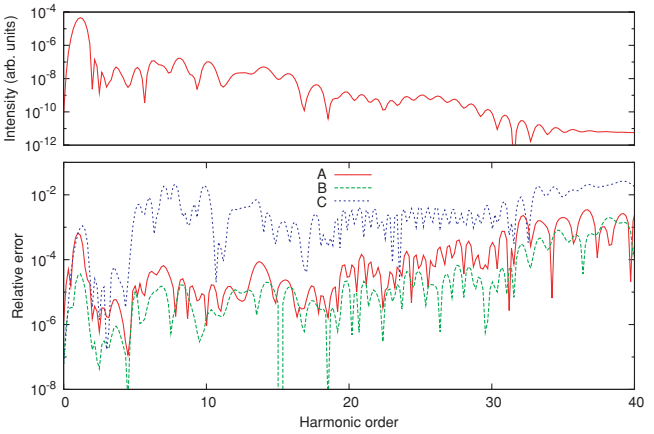

FIG. 6. (Color online) High harmonic power spectrum from the H atom for a one-cycle pulse (upper panel). Lower panel: Error $\mathcal{D}(\omega)$ with irECS parameters $(R_0,M_A,\theta,\alpha)=(40,20,0.5,0.5)$ relative to a $R_0=80$ calculation (curve A). The relative difference to a calculation with (40,40,0.4,0.4), curve B, underestimates the error. The calculation is converged with 20 angular momenta on the given level of accuracy. More angular momenta do not change the result. At 15 angular momenta (curve C) accuracy deteriorates.

than this irrespective of discretization and scaling parameters. Again this error is related to the numerical limits of our discretization and propagation schemes: the wave-function error is $\sim10^{-7}$ and the high frequency signal is suppressed by 10^{-4} relative to the fundamental peak, making a relative error of the suppressed signal of the order 10^{-3} quite plausible. Indeed we find similar errors when comparing different, but equally accurate purely real calculations. More disquieting is the $\sim1\%$ error at the fundamental frequency, which does not appear in large-box real calculations. We were not able to locate the origin of this error: It persists through variations of R_0, specific discretizations, different time discretizations, and also for the three-dimensional H calculation in the following (cf. Fig. 6). The error appears to be related to an artificial overall modulation of the signal by the driving field, possibly related to internal normalizations during propagation. Note that by construction normalization errors do not appear in the wave-function accuracy measure $\mathcal{E}$, Eq. (3). We believe, however, that this error is acceptable for all practical purposes.

G. irECS fails in length gauge

For field interaction in length gauge

$$i\vec{A}(t)\vec{\nabla}_{\vec{x}} \to \vec{x}\frac{d\vec{A}}{dt}, \tag{30}$$

irECS completely fails in the time-dependent case. The reason for this behavior was pointed out in Ref. [6]: When length-gauge Volkov solutions are complex scaled their asymptotic behavior becomes dependent on the sign of the field strength and alternates between damping and growth. The convenient distinction between incoming and outgoing waves by their norms is lost. In the language of mathematical theory, $\vec{x}$ is not a dilation analytic potential and severely so: complex scaling transforms the spectrum of the Stark problem from purely

TABLE V. Parameters for the Ne model potential Eq. (32).

	a_i	c_i
1	−1	0
2	−0.3	0.5
3	−2.05	2
4	1.23	1

continuous into purely discrete and all discrete eigenvalues of the scaled Stark Hamiltonian have imaginary parts [15]. This is in sharp contrast to dilation analytic potentials where the bound-state energies remain unchanged and the continuous spectrum is only rotated into the lower complex plane.

VI. CALCULATIONS FOR H AND MODEL NE

To demonstrate the applicability of irECS to realistic problems, we show calculations for the H atom with

$$V(\vec{x}) = -\frac{1}{|\vec{x}|}, \tag{31}$$

and a single electron model of the Ne atom with the potential

$$V(\vec{x}) = \sum_{i=1}^{4} a_i \frac{\exp[-c_i|\vec{x}|]}{|\vec{x}|}. \tag{32}$$

We use the parameters given in Table V, for which our model reproduces the ground and first few excited state energies of Ne. We use linearly polarized pulses with the same pulse shape and peak intensity as in the preceding section and pulse durations of 1 and 10 optical cycles. The calculations are done in polar coordinates with a spherical harmonics basis on the angular coordinates and high-rank finite elements on the r coordinate. Again, an infinite last element is used.

There are no surprises: Convergence patterns and accuracy are very similar to the one-dimensional model. Figure 6 shows the harmonic spectrum for H at one cycle together with errors for different irECS and discretization parameters. The error estimate here is by comparison to an $R_0 = 80$ calculation.

No new problems appear due to the more general Ne model potential (32). Figure 7 shows high harmonic spectra from an H and Ne for a 10-cycle pulse. Accuracy estimates were obtained by varying the irECS radius R_0.

VII. DISCUSSION

As we find high numerical stability and excellent performance of irECS as an absorber, the questions arise as to what are the reasons for the numerical problems reported in Refs. [4,5], where ECS was applied to essentially the same systems. One obvious source of inaccuracies may lie in possible low-order discretizations. Unfortunately, in neither publication is an investigation of the dependence of the observed effects on discretization shown.

We have documented the generally poorer performance of ECS compared to irECS, but according to Table II with the very large absorption ranges of 80 Bohr used in Ref. [5], excellent results should be achievable also in ECS. Note that this absorption range is twice as large as the unscaled range.

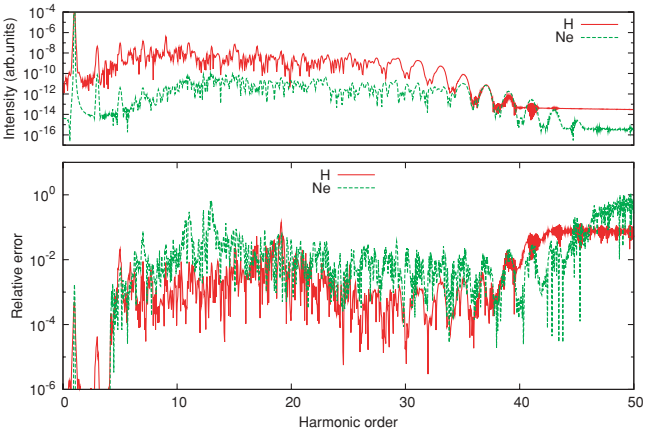

FIG. 7. (Color online) High harmonic power spectra from the H and an Ne model with a 10-cycle pulse (upper panel). Relative accuracies shown in the lower panel are somewhat poorer with the longer pulse, in particular for Ne where due to the higher ionization potential the signal is very weak.

A possible source of the observed difficulties may be the treatment of the overlap matrix. As discussed previously we replace the ordinary overlap by the pseudo-overlap matrix $\hat{S}_{\theta R_0}$. With this choice, and as we use strictly real finite element functions, we obtain complex symmetric matrices $(\hat{H}_{\theta R_0})^T = \hat{H}_{\theta R_0}$ for zero field $A_0 = 0$ and $(\hat{S}_{\theta R_0})^T = \hat{S}_{\theta R_0}$. There are no explicit statements about $S_{\theta R_0}$ in Refs. [4,5]. Usually, finite-difference methods imply (an approximation to) the identity operator for overlap. The B-spline method used in [5] requires a choice for $S_{\theta R_0}$ and Eq. (20) of Ref. [5] seems to imply that indeed the identity was used as an overlap matrix.

The comment on the nonorthogonality of the eigenvectors of the nonnormal scaled Hamiltonian in [5] also seems to indicate that the ordinary, unscaled overlap matrix $\hat{S}$ was used. Clearly, the eigenvectors $\vec{b}^{(\alpha)}$ of the eigenproblem

$$\hat{H}_{\theta R_0}\vec{b}^{(\alpha)} = \hat{S}\vec{b}^{(\alpha)}E_\alpha, \tag{33}$$

will not be orthogonal in general. However, we find that all eigenvectors of the complex-scaled generalized eigenproblem

$$\hat{H}_{\theta R_0}\vec{c}^{(i)} = \hat{S}_{\theta R_0}\vec{c}^{(i)}E_i, \tag{34}$$

are pseudo-orthogonal and can be normalized in the sense

$$\sum_{lm} c_l^{(i)}(\hat{S}_{\theta R_0})_{lm}c_m^{(j)} = \delta_{ij}. \tag{35}$$

Then the matrix $\hat{H}_{\theta R_0}$ has a diagonal representation

$$\hat{H}_{\theta R_0} = \sum_i \vec{c}^{(i)}E_i(\vec{c}^{(i)})^T, \tag{36}$$

and the spectral values E_i appear as discrete approximations to the true irECS spectrum with strictly nonpositive imaginary parts $\mathcal{I}mE_\alpha \leqslant 0$. We do not have mathematical proof for this property of the discrete complex-scaled system, but we find it valid in all our calculations on the level of computational accuracy. If, on the other hand, we use the ordinary overlap matrix $\hat{S}$, we invariably obtain a few eigenvalues E_α with $\mathcal{I}mE_\alpha > 0$ which will cause long-term instability of the

time propagation. Possibly this is the ultimate reason for the numerical instabilities observed in Refs. [4,5].

VIII. SUMMARY

We have demonstrated that irECS can serve as a perfect absorber of outgoing flux in the sense that in the unscaled inner region it exactly matches a purely real calculation on a sufficiently large grid. With between only 20 to 40 absorption points, we were able to push the agreement to relative $\mathcal{L}^2$ error of 10^{-15}. The corresponding errors in the wave-function amplitude are $\sim 10^{-7}$. Both errors are at the limits of our numerical integration scheme. Furthermore, we have evidence that irECS does not just act as an absorber, but conserves dynamical information during excursions into the absorbing region: Even when the quiver motion takes flux deeply into the "absorbing" region, the returning flux is identical to the flux in a purely real calculation. We believe that irECS solves the absorption problem for the present class of system.

For this, we found the following points essential:

(i) implementation of the correct scaled derivatives, including bra functions with unconjugated discontinuity;

(ii) the use of "infinite" absorption ranges, which we discretized by polynomials times an exponential; and

(iii) the use of high-rank discretization also in the inner region to reach the highest accuracies.

Point (i) leads to a complex symmetric, in particular, not a positive-definite discrete overlap matrix which must not be approximated by a positive-definite matrix.

Following these rules, we encountered no numerical difficulties in the inner region or in the absorbing region, using a standard explicit Runge-Kutta scheme for time integration. As a tendency, large scaling angles favor good absorption, in many cases we used $\theta = 0.7 \approx 40^\circ$, which corresponds to an almost purely imaginary continuous energy spectrum $[0, e^{-2i\theta}\infty)$. In our basis we found the scaling angle ultimately to be limited by numerical instabilities due to the complex symmetric overlap matrix. As excellent absorption can be achieved with as few as 20 discretization coefficients in the absorbing region, pushing the scaling angle to the numerical limits is not necessary, in general, and scaling angles of $\theta = 0.3 \sim 0.5$ served well for our purposes. In general, we found the scheme numerically robust and not very sensitive to the scaling parameters. The option of back-scaling the solution to $\theta = 0$ was abandoned due to severe cancellation errors in the related transformations.

When judging the accuracy of an irECS calculation, it is important to vary the irECS radius R_0. Our comparison with a real calculation indicates the variation of the result with different R_0 gives realistic error estimates. Other parameters such as rank of the finite elements, length of the absorption range, or scaling angle are of secondary importance.

Both, ECS and irECS, outperform simple monomial CAP's. ECS errors were one or two orders of magnitude smaller than CAP errors with the same spatial discretization, but the advantage of irECS can reach 12 orders of magnitude! We are aware of the fact CAP's can be greatly improved by a variety of measures (see, e.g., [16]). However, in general, these require tuning of the CAP parameters to a given situation. Even with that, we do not expect to reach comparable accuracies with CAP's as we could demonstrate for irECS.

The efficiency and excellent performance of irECS can serve to dramatically reduce the effort for computing photoionization processes and opens new possibilities for simulation. Short absorption ranges become crucial for few-particle systems, where overall absorbing volume grows exponentially with the number of particles. Further, a perfect absorber is the prerequisite to be able to extract scattering information from simulations in a small finite volume. Such a scheme was formulated in Ref. [17] for laser-ionization using CAP's. An adaptation to irECS and its extension to few-body dynamics will be investigated in future work.

ACKNOWLEDGMENTS

This work was supported by the Viennese Science Foundation (WWTF) via the project "TDDFT" (MA-45). The author acknowledges support by the STSM program of COST action CM0702.

APPENDIX: CONSTRUCTION OF THE BASIS

Here we show explicitly how to construct the finite element basis sets used in this paper. On a given element $[x_{n-1}, x_n]$ we choose a set of functions $h_i^{n)}(x), i = 1, \ldots, p_n$. We define the $2 \times p_n$ matrix of boundary values $B_{bi} = h_i^{(n)}(x_{n+b-2}), b = 1,2$. We require that B has at least two linearly independent columns, let us assume for notational simplicity that these are the first and last columns. Be C the 2×2 matrix of the first and last columns of B. It is easy to see that the new basis set $g_i^{(n)}, i = 1, \ldots, p_n$

$$g_1^{(n)}(x) = (C^{-1})_{11} h_1^{(n)}(x) + (C^{-1})_{12} h_{p_n}^{(n)}(x), \tag{A1}$$

$$g_{p_n}^{(n)}(x) = (C^{-1})_{21} h_1^{(n)}(x) + (C^{-1})_{22} h_{p_n}^{(n)}(x), \tag{A2}$$

$$g_i^{(n)}(x) = h_i^{(n)}(x) - B_{1i} g_1^{(n)}(x) - B_{2i} g_{p_n}^{(n)}(x), \quad i = 2, \ldots, p_n - 1, \tag{A3}$$

fulfills the conditions in Eq. (17). Note that the only requirement on the original functions is that C is invertible (i.e., the boundary value matrix has at least two linearly independent columns).

We transform to the form of Eq. (18) by first obtaining an orthonormal set of inner functions $f_i^{(n)}, i = 2, \ldots, p_n - 1$ $\langle f_i^{(n)} | f_i^{(n)} \rangle = \delta_{ij}$ from $g_i^{(n)}, i = 2, \ldots, p_n - 1$ (e.g., by Schmidt orthonormalization). We then remove the content of all inner $f_i^{(n)}$ from the boundary functions $g_1^{(n)}$ and $g_{p_n}^{(n)}$ by the projection

$$f_b^{(n)} = (1 - P_I) g_b^{(n)}, \quad b = 1, p_n, \tag{A4}$$

with the projector $P_I = \sum_{i=2}^{p_n - 1} |f_i^{(n)}\rangle\langle f_i^{(n)}|$. As the inner functions are equal to zero at the element boundaries, the boundary conditions in Eq. (17) remain unaffected by these transformations. All transformations can be performed quickly and reliably during setup by computing the matrices $T_{ij}^{(n)}$ that directly take the $h_j^{(n)}$ to $f_i^{(n)} = \sum_{j=1}^{p_n} T_{ij}^{(n)} h_j^{(n)}$. Mathematically speaking, the spaces spanned by $h_i^{(n)}$ and $f_i^{(n)}$ are identical, but

the latter form is nearly orthogonal and therefore numerically stable and in addition allows for convenient implementation of the continuity conditions across boundaries.

The manipulations for the infinite end elements are almost identical, except that now the boundary matrix B is $1 \times p_n$ and a single nonzero entry in B is sufficient.

As $h_i^{(n)}$ we choose scaled and shifted Legendre polynomials $h_i^{(n)} = P_i[y_n(x)]$, where y_n maps $[x_{n-1},x_n]$ onto $[-1,1]$

$$y_n(x) = \frac{2x - x_{n-1} - x_n}{x_n - x_{n-1}}. \tag{A5}$$

On the end elements we start from Laguerre polynomials with arguments scaled by $\pm 2\alpha$ times the exponentials $\exp(\pm\alpha x)$ on the lower and upper ends, respectively. Mathematically speaking, the choice of polynomials is irrelevant as long as all orders up to p_n are included. However, for monomials $h^{(n)}(x) = (x - x_{n-1})^i$, the transformations will breakdown for numerical reasons already at ranks $p_n \sim 10$. Starting from orthogonal polynomials eliminates all ill-conditioning problems in the various transformations.

With this, the basis sets are completely defined up to a numerically irrelevant orthogonal transformation among the inner functions, if the element boundaries x_n, the rank p_n, and, where applicable, the exponent α is given. In the one-dimensional calculations we used constant size elements. For the Coulomb problem, the element sizes started from $x_1 - x_0 = 0.3p_n$ and then increased linearly up to the radius 15. Beyond that the element size was kept constant. We obtain the first few H bound states to machine accuracy. What mainly determines the good accuracy is the high p_n used. The use of a variable size element is routine to our implementation, but not relevant for the findings.

[1] X. Antoine, A. Arnold, C. Besse, M. Ehrhardt, and A. Schädle, Comm. Comp. Phys. **4**, 729 (2008).

[2] J. L. Krause, K. J. Schafer, and K. C. Kulander, Phys. Rev. A **45**, 4998 (1992).

[3] U. V. Riss and H.-D. Meyer, J. Chem. Phys. **105**, 1409 (1996).

[4] F. He, C. Ruiz, and A. Becker, Phys. Rev. A **75**, 053407 (2007).

[5] L. Tao, W. Vanroose, B. Reps, T. N. Rescigno, and C. W. McCurdy, Phys. Rev. A **80**, 063419 (2009).

[6] C. W. McCurdy, C. K. Stroud, and M. K. Wisinski, Phys. Rev. A **43**, 5980 (1991).

[7] E. Balselev and J. Combes, Commun. Math. Phys. **22**, 280 (1971).

[8] J. Aguilar and J. Combes, Commun. Math. Phys. **22**, 269 (1971).

[9] M. Reed and B. Simon, *Methods of Modern Mathematical Physics* (Academic, New York, 1982), p. 183ff.

[10] C. Nicolaides and D. Beck, Phys. Lett. A **65**, 11 (1978).

[11] B. Simon, Phys. Lett. A **71**, 211 (1979).

[12] C. McCurdy, M. Baertschy, and T. Rescigno, J. Phys. B **37**, R137 (2004).

[13] A. Scrinzi and N. Elander, J. Chem. Phys. **98**, 3866 (1993).

[14] A. Scrinzi and B. Piraux, Phys. Rev. A **58**, 1310 (1998).

[15] I. W. Herbst, Commun. Math. Phys. **75**, 197 (1980).

[16] J. Muga, J. Palao, B. Navarro, and I. Egusquiza, Phys. Rep. **395**, 357 (2004).

[17] J. Caillat, J. Zanghellini, M. Kitzler, O. Koch, W. Kreuzer, and A. Scrinzi, Phys. Rev. A **71**, 012712 (2005).